ANL-HEP-PR-99-01

Analyzing powers for the $\pi^- \vec{p} \to \pi^0 n$ reaction across the $\Delta(1232)$ resonance

C. V. Gaulard,[1*] C. M. Riedel,[2†] J. R. Comfort,[1] J. F. Amann,[2] M. E. Beddo,[3‡] R. L. Boudrie,[2] G. R. Burleson,[3] P. L. Cole,[4§] K. K. Craig,[1] M. A. Espy,[5‖] L. D. Isenhower,[6] T. E. Kasprzyk,[7] K. R. Knight,[6] C. L. Morris,[2] S. Penttilä,[2] D. Rigsby,[6] M. E. Sadler,[6] E. Six,[1] H. M. Spinka,[7] I. Supek,[8] G. J. Wagner,[9] Q. Zhao[3¶]

[1] *Arizona State University, Tempe, Arizona 85287*
[2] *Los Alamos National Laboratory, Los Alamos, New Mexico 87545*
[3] *New Mexico State University, Las Cruces, New Mexico 88003*
[4] *George Washington University, Washington DC 20052*
[5] *University of Minnesota, Minneapolis, Minnesota 55455*
[6] *Abilene Christian University, Abilene, Texas 79699*
[7] *Argonne National Laboratory, Argonne, Illinois 60439*
[8] *Rudjer Boskovic Institute, 41000 Zagreb, Croatia*
[9] *Universität Tübingen, D-72076 Tübingen, Germany*

(December 21, 1998)

High quality analyzing powers for the $\pi^- \vec{p} \to \pi^0 n$ reaction have been obtained with a polarized proton target over a broad angular range at incident kinetic energies of 98.1, 138.8, 165.9, and 214.4 MeV. This experiment nearly doubled the existing πN single-charge-exchange database for energies ranging from 10 to 230 MeV, with 36 new analyzing powers. The Neutral Meson Spectrometer was used to detect the outgoing neutral pions. The data are well described by recent phase-shift analyses. When combined with high-precision and accurate cross section data at the same energies, the data can provide a good test of the degree of isospin breaking in the region of the $\Delta(1232)$ resonance. They will also be helpful for constraining the evaluation of the pion-nucleon sigma term from the scattering amplitudes.

PACS numbers: 25.80.Gn, 24.70.+s, 13.75.Gx

I. INTRODUCTION

The pion-nucleon interaction has a fundamental role in understanding nuclear reactions, in describing the structure of nuclei, and in providing a window into fundamental issues of the structure of the nucleon.

Although there have been many experiments for the $\pi^- p \to \pi^0 n$ reaction above the $\Delta(1232)$ resonance at several different laboratories, the current status of the database and associated phase-shift analyses below the $\Delta(1232)$ resonance is still very cloudy. Accurate single-charge-exchange (SCX) measurements will significantly help to enhance the πN database, and therefore will contribute to an unambiguous decomposition of the πN amplitudes. Alternatively, they are also needed to determine the degree of isospin-symmetry breaking in the πN system so that the amplitudes can be treated in a fully consistent framework. Polarization measurements are particularly sensitive to the interference between partial waves, and thus help to constrain the partial-wave decompositions of the scattering amplitudes. A solid πN data base may be used to determine the πNN coupling constant, test isospin-symmetry breaking, and constrain the estimate of the strange-quark content of the nucleon through extraction of the pion-nucleon sigma term.

The QCD Lagrangian may be expressed in terms of a part $\mathcal{L}_0$ which is chirally invariant and depends exclusively on the quark and gluon color fields, and a quark mass term: $\mathcal{L}_{QCD} = \mathcal{L}_0 + \Delta\mathcal{L}$. The quark mass term

$$\Delta\mathcal{L} = -\sum_q m_q \bar{\psi}^i_q \psi_{qi} \,, \tag{1.1}$$

where m_q is the quark mass and ψ_{qi} is the quark field of flavor q and color i, breaks chiral symmetry. At low energies and considering only the two lightest quarks,

$$\Delta\mathcal{L} = -(m_u \bar{u}u + m_d \bar{d}d) \tag{1.2}$$

$$= \frac{1}{2}(m_u + m_d)(\bar{u}u + \bar{d}d) + \frac{1}{2}(m_u - m_d)(\bar{u}u - \bar{d}d) \,. \tag{1.3}$$

The first (isoscalar) term of Eq. 1.3 yields the sigma term σ, which is a measure of explicit chiral symmetry breaking. The second (isovector) term breaks isospin invariance. It depends not only on the mass difference of the up and down quarks, but also on the difference in the respective quark condensates.

Work supported in part by the U.S. Department of Energy, Division of High Energy Physics, Contract W-31-109-ENG-38.

The πNN coupling constant sets the scale for hadronic interactions. The long-standing historical value $g_c^2 = 14.3 \pm 0.2$ was obtained from phase-shift analyses of charged $\pi^+ p$ and $\pi^- p$ scattering [1]. Recently, careful phase-shift analyses of NN and $\overline{NN}$ scattering data by the Nijmegen group have resulted in lower values, near 13.5 [2]. Unlike earlier suggestions [3,4], there appears to be little difference between the charged coupling g_c^2 (from I=1 np scattering) and the neutral coupling g_0^2 (from pp scattering). Very similar results were found by the Virginia Polytechnic Institute (VPI) group [5] and by Timmermans [6] in phase-shift analyses of πN data. The VPI value is $g^2 = 13.75 \pm 0.15$, again without dependence on the charge state. A separate analysis of low-energy πN data in a potential model also yields a value near 13.7 [7]. However, Ericson et al., analyzing np-scattering data taken at Uppsala, have found a value $g_c^2 = 14.6$, higher than the historical Karlsruhe-Helsinki value [8]. In contrast, Ericson and Loiseau have obtained a value $g^2 = 13.0 \pm 0.7$ from an analysis of CERN $\bar{p}p \to \bar{n}n$ data [9].

The issue is unsettled and remains controversial. If the analysis of the Uppsala data is disregarded, the current results on the πNN coupling constant provide no evidence for the breaking of charge independence. On the other hand, other analyses of low-energy data, comparing SCX amplitudes derived from SCX data with those predicted from recent $\pi^{\pm} p$ elastic data, have provided empirical evidence that isospin symmetry is indeed broken in the πN system beyond the usual Coulomb effects and pion or nucleon mass differences [7,10]. High-precision polarization data will further constrain the partial-wave analyses, and thereby help determine whether evidence for this extra degree of isospin-symmetry breaking also extends across the $\Delta(1232)$ resonance.

Although the common picture of nucleons is that they are composed of only up and down quarks, there is considerable current interest as to whether there is also a substantial strange quark content. Relevant evidence can be found in the sigma term, which is renormalized by the strange quarks. One estimate of σ is obtained from the baryon mass spectrum [11]. Another estimate comes from the $\Sigma_{\pi N}$ term which is obtained via πN phase-shift analyses by extrapolating the isospin-even amplitude to the unphysical Cheng-Dashen point [12]. The consistency of the two estimates is very much an open issue and a subject of continuing discussion. Although the extrapolation is made with isospin-even amplitudes, while the SCX reaction is entirely isospin-odd, SCX data can still play an important role in the determination of $\Sigma_{\pi N}$, because $\pi^{\pm} p$ processes have mixtures of both isospin-even and isospin-odd terms. The SCX reaction isolates the isospin-odd terms without the additional complication of coherent Coulomb scattering amplitudes.

The motivation for this experiment is thus twofold. First, if isospin is rigorously good, the additional information provided by the SCX polarization measurements will help to constrain phase-shift analyses at energies near and below the $\Delta(1232)$ resonance and thus improve our knowledge of the coupling constants as well as the extrapolated value of the $\Sigma_{\pi N}$ term. On the other hand, if isospin invariance is broken, the SCX reaction is not determined by the $\pi^{\pm} N$ scattering and it *must* be studied as a separate process. In fact, Weinberg has noted that isospin breaking may make sizeable contributions to the $\Sigma_{\pi N}$ term, comparable to those from chiral-symmetry breaking [13].

Compared to the elastic πN database, information for the SCX channel is rather sparse, and there is a strong need for more πN analyzing-power SCX data below the $\Delta(1232)$ resonance. For scattering to beam left, the analyzing power is defined as

$$A_y = \frac{\left(\frac{d\sigma}{d\Omega}\right)_{\uparrow} - \left(\frac{d\sigma}{d\Omega}\right)_{\downarrow}}{P_{\downarrow}\left(\frac{d\sigma}{d\Omega}\right)_{\uparrow} + P_{\uparrow}\left(\frac{d\sigma}{d\Omega}\right)_{\downarrow}}, \tag{1.4}$$

where $P_{\uparrow}$ ($P_{\downarrow}$) are the measured up (down) target polarizations. The variables $(d\sigma/d\Omega)_{\uparrow}$ and $(d\sigma/d\Omega)_{\downarrow}$ are the respective differential cross sections from the spin-up and spin-down spectra. In addition to cross sections, the measurement of analyzing powers has the advantage that it doubles the number of independent experimental quantities that are used in phase-shift analyses. Furthermore, analyzing powers provide important information on the relative phases between the spin-independent and spin-dependent terms in the effective πN interaction. The enhanced sensitivity to the terms of the πN interaction is essential for resolving the issues mentioned above.

II. EXPERIMENTAL APPARATUS

Experiment E1178 measured analyzing powers A_y for the SCX reaction $\pi^- \vec{p} \to \pi^0 n$ over a broad angular range at incident pion energies from 98.1 to 214.4 MeV. The energies correspond to those where $\pi^{\pm} p$ analyzing powers [14,15] have been measured. The experiment was carried out at the Low Energy Pion (LEP) channel of the Clinton P. Anderson Meson Physics Facility (also known as the Los Alamos Meson Physics Facility, LAMPF) with a dynamically polarized proton target. The scattered neutral pions were detected by the Neutral Meson Spectrometer [16]. A floor layout, with a typical arrangement of the spectrometer and of the magnets, is shown in Fig. 1.

A. Low Energy Pion channel

The LEP channel was designed to provide $\pi^{\pm}$ beams from about 10 MeV through the resonance region ($\sim$ 300 MeV) with variable beam momentum spread $\Delta p/p$ from $\pm$ 0.05 to $\pm$4%. A detailed description of the LEP channel is provided by Refs. [17,18].

During experiment E1178 the typical values of $\Delta p/p$ ranged from 0.3% to 3.0%, corresponding to a pion flux of up to about 10^7 π/s. The duty factor was about 6%. The choice of momentum bites was based solely on limiting the singles rates in the detectors, particularly in the CsI crystals (see Sect. II C), to a workable range of the data acquisition system.

1. Extended beam line

In order to install the target and its associated apparatus inside the experimental area, an extended beam line that consisted of two quadrupoles and one dipole (Werbecka) magnet was installed at the channel exit, as sketched in Fig. 2. The purpose of the Werbecka dipole magnet was to steer the pion beam away from the standard beam line in order to compensate for the bending effect of the target polarizing magnet (Zoltan). The field of Werbecka was adjusted until the charged pion beam passed through the center of Zoltan, hitting the target at approximately 0° with respect to its normal. The locations of the additional magnets relative to the last channel quadrupole doublet and the strengths of their field settings were calculated with the code TRANSPORT [19], and the fields were adjusted on-line. The accuracy of the steering was checked by placing polaroid film at the center of the Zoltan field, so as to obtain an image of the beam at the target location.

2. Beam tune and beam monitoring

All of the settings of the magnets of the LEP channel were calculated with the program TRACE. The quadrupoles were then fine-tuned to obtain the smallest beam spot at the target position. For this experiment, the beam spot was usually $\sim$ 1 cm $\times$ 1.5 cm in diameter (the widest side being oriented horizontally). The optimal beam-collimator openings were determined individually by looking at the beam flux, i.e. the beam envelope at each collimator was cut until the nominal beam intensity was separately reduced by about 10%. The beam energy is believed to be accurate to better than 1 MeV, a value consistent with some direct time-of-flight measurements that were made.

The incident beam flux was monitored with two independent beam monitors: an ion chamber recording the current produced by the passage of the beam particles just before the Zoltan magnetic field area (Fig. 2), and two toroid coils located on the primary proton beam line. Because the measurement of analyzing powers does not require knowledge of the absolute pion beam flux, it was not necessary to determine the fractions of electrons and muons in the beam, but they were typically at the few percent level or less.

B. Polarized proton target

The protons in the target material were polarized by using the Dynamic Nuclear Polarization (DNP) method. DNP is obtained through the dipolar coupling with electron spins by placing a sample containing protons and unpaired electrons into a homogeneous magnetic field at low temperatures and applying a suitable microwave field to it with a frequency near the electron spin resonance frequency. The high electron polarization can then be transfered to the proton. The absolute polarization of protons is determined by using the nuclear magnetic resonance technique. Fig. 3 shows the target setup and the nose part of the refrigerator between the poles of the Zoltan magnet.

1. Dynamic nuclear polarization method

A detailed description of the DNP method can be found in Refs. [20–22] and in a recent review article [23]. In order to polarize the protons, a homogeneous external magnetic field is needed to lift the magnetic-substate degeneracy of the nucleus. A strong magnetic field with high homogeneity ($\Delta B/B \leq 10^{-4}$ over the target volume) was provided by the Zoltan iron-core C-magnet.

The thermal equilibrium polarization for a spin-1/2 nucleus is given by

$$P = \tanh(\mu B/kT) \ , \tag{2.1}$$

where μ is the magnetic dipole moment and k is the Boltzmann constant. For a field $B = 2.5$ T and a temperature of 0.5 K, near the typical operating conditions, the polarization of the proton is about 0.5%, while the polarization of electrons is nearly 100%. The DNP technique is used to enhance the proton polarization by transferring the electron polarization to the proton. At the low temperature and high magnetic field cited above, the relaxation time of the electron spin is of the order of milliseconds, while that the proton spin is normally several seconds or more. This ratio allows the proton spin to remain in an enhanced state while the electron relaxes back so that it can absorb a photon from the microwave field and flip another proton spin. Continuous enhancement is required in order to maintain an overall target polarization.

The microwaves of the DNP process were supplied through a waveguide to the target located in the mixing chamber of a dilution refrigerator. The teflon target holder which contained the target beads was placed in a copper can that served as a multimode microwave cavity. The target beads were continuously irradiated by microwaves of about 69-70 GHz during the data acquisition in order to achieve a steady-state polarization. Changing the microwave frequency by about 425 MHz reversed the sign of the polarization. No changes in the external magnetic field were required, thus keeping systematic errors to a minimum.

2. Nuclear Magnetic Resonance system

A Nuclear Magnetic Resonance (NMR) system [22,24] was used to monitor and measure the absolute proton polarization of the target material. Such measurements in two different conditions are required: at Thermal Equilibrium (TE) and in the enhanced polarization mode. To obtain a normalized measurement, the enhanced polarization must be calibrated against the TE NMR measurement whose polarization is known from Boltzmann statistics (see Eq. 2.1). The proton polarization at 1 K where the TE measurements were done, and in a field of 2.5 T, is approximately 0.25 %.

Because the area under the peak of the NMR spectrum is proportional to the polarization, it can be used to determine the enhanced polarization. Therefore, by measuring the area for the proton system at TE ($A_{\rm TE}$), the enhanced polarization (P) can be calculated from the expression

$$P = P_{\rm TE}\frac{A}{A_{\rm TE}} \ . \tag{2.2}$$

The TE calibrations were done about once a week during the experiment.

In this experiment, some corrections to the scaled polarization values were needed. Large modulations of the base RF level of the NMR circuit can lead to nonlinear NMR signals and asymmetric polarization values. The modulations arise from changes in the sampling-coil impedence as a result of strong couplings of the NMR signal to the proton magnetic moments. The non-linearities of the NMR circuit were modeled from carefully measured parameters, and the polarization values obtained from Eq. 2.2 were corrected. Full details are given elsewhere [25]. The averages of the proton polarization over this experiment were about $\langle P_\uparrow \rangle \simeq 90 \pm 4.5\%$ and $\langle P_\downarrow \rangle \simeq 80 \pm 4.5\%$, ($\pm 4.5\%$ is the overall target polarization uncertainty; see Sect. III D).

3. Dilution refrigerator

The low temperatures required for the DNP were achieved with a ^{3}He-^{4}He dilution refrigerator [26] of the CERN type [27,28]. It was specifically modified for this experiment to reduce the thicknesses of the cryostat walls and for the use of polarized target experiments with the LAMPF beam. It can be operated in a horizontal mode as in this experiment, or vertically. The loading of the target material, which needs to be done at or below liquid nitrogen temperature, can be done directly into the mixing chamber.

4. Target material

The compound 1-butanol $CH_3(CH_2)_2CH_2OH$ was chosen as target material because of its chemical composition. It has the advantage of being rich in polarizable hydrogen with a minimum of elements with non-zero nuclear spin. The only significant polarized background is created by ^{13}C. The approximate 1.1% abundance of ^{13}C in natural carbon will be polarized to about 28-30% when the proton polarization is about 80-90%. This carbon polarization will produce

a small asymmetry, but less than the systematic errors from other sources. The natural abundance of the ^{17}O of about 0.04% is negligible. The target material also has one of the best ratios of hydrogen to contaminant carbon and oxygen atoms of all suitable materials, which helps to reduce backgrounds. Distilled water at 5% by weight was added to the 1-butanol in order to increase the polarization [29]. The target material was doped with 5×10^{19} atoms/cm^3 of EHBA-Cr(V) complex (paramagnetic complex sodium bis(2-ethyl-2-hydroxybutyrato)oxochromate(V)monohydrate), which is soluble in butanol [30]. EHBA-Cr(V) provides unpaired electrons in order to create a stable and homogeneous distribution of polarizing centers throughout the target volume. These paramagnetic centers are uniformly-distributed and fixed in place when the Cr(V) complexes are frozen into the butanol. It is not necessary for the target material to be fully paramagnetic; only the concentration level and the uniformity of the distribution of the free spins is important.

The target material was prepared in the form of frozen beads of about 1-1.5 mm diameter in order to improve the thermal contact with the ^{3}He-^{4}He bath. The target container was a rectangular perforated teflon basket enclosed in a copper microwave cavity immersed into a mixture of ^{3}He and ^{4}He liquids. The copper cavity also served as the container for the ^{3}He-rich phase. Great care was taken to exclude hydrogen from the target vicinity; otherwise the NMR calibrations would have had a systematic error. The dimensions of the teflon basket were: height $\times$ length $\times$ thickness $= 2.5 \times 5 \times 1.7$ cm^3.

Because the hydrogen peak in the energy spectrum of the outgoing π^0's sits on top of a broad background due to the contaminant materials of the target and of the cryostat, a second target was made to provide data in order to determine the spectral shape of this background. A hydrogen-free target consisting of graphite (C) and of "dry ice" beads (CO_2) was used for background subtraction. The quantities each of graphite and of "dry ice" were chosen such that the effective thicknesses of carbon and oxygen in the background target were similar to the ones in the butanol target; see Tables I and II. Because the effect of the geometry of the target cannot be neglected, it was important to build a background target as close as possible to the geometry of the polarized target. The background target had a teflon basket identical to that of the polarized target, but with a thickness of 0.8 cm instead of 1.7 cm in order to obtain the same effective areal thickness of carbon and oxygen.

C. Neutral Meson Spectrometer

The neutral pions from the $\pi^- \vec{p} \to \pi^0 n$ reaction were detected in the Neutral Meson Spectrometer (NMS). With a mean lifetime at rest of 0.84×10^{-16}s, the π^0 decays instantaneously within the target in which it is produced. Only the dominant electromagnetic decay mode $\pi^0 \to \gamma\gamma$, which proceeds with a branching ratio of $98.798 \pm 0.032\%$ [31], is detected.

1. Neutral Meson Spectrometer design

The presence of a π^0 must be inferred from the observation of its decay products. The NMS therefore consists of two identical detectors operating in coincidence mode to detect the two photons from the neutral meson decays. A sketch of the NMS is given in Fig. 4.

The two detectors of the NMS are independent position-sensitive, high-energy, γ-ray detectors. The front face of each detector is a plane of fifteen 0.95-cm-thick plastic scintillators which veto any incoming charged particles. This veto plane is followed by two identical conversion systems. Each system consists of an active bismuth germanate (BGO) converter plane followed by a tracking wire-chamber package. Each γ-ray can convert in either one of the two active converter planes into an electromagnetic shower. The electrons and positrons exiting the back of each converter plane are detected in the wire chambers, and this information is used to determine the conversion point coordinates of the e^+e^- vertex and thus the opening angle η of the π^0 decay. This vertex position and opening-angle determination is the measurement which is the most critical for achieving good resolution. At the back of each detector is a 6×10 array of pure cesium iodide (CsI) crystals which serve as a photon calorimeter. The total shower energy in each arm is determined by adding the signal from the calorimeter to the energy deposited in the active converter planes. The support structure of each detector was designed to permit the independent placement of each detector in the reaction plane. The shape of the structure allowed each detector to be placed very close to the target in order to optimize the count rate.

The γ-ray direction is defined by a line between the conversion point in each detector and the center of the target (see Fig. 4). Thus each detector measures independently the three kinematic variables of one photon: energy E_γ, polar angle θ_γ, and azimuthal angle ϕ_γ. The combined information from the two detectors over-determines the π^0 decay kinematics. It is completely described with the following variables: energy sharing parameter X, opening angle η, π^0 energy E_{π^0}, and scattering angle θ_{π^0}, as discussed in the following section.

a. Bismuth Germanate converters Each converter plane is composed of 28 strips (arranged in a 2 × 14 array of BGO crystals) with each strip coupled to a light guide and a photomultiplier tube. The dimensions of the total active area are 40.64 cm × 71.12 cm × 0.635 cm. The dimensions of the converter planes were chosen so as to cover the wire chambers. The overall conversion efficiency was increased by using two converter planes, separated by tracking wire chambers. The conversion efficiency is defined as the probability that an incident γ-ray results in at least one charged particle that exits the back face of the converter and is tracked in the wire chambers.

The conversion efficiency also depends on the thickness of the converters. However, an excessive increase of the thickness will increase the probability that the charged particles created in the converter are totally absorbed before they emerge. On the other hand, a converter that is too thin will reduce the light collection from it. Monte-Carlo studies of this problem gave an optimal converter thickness of about 0.5 radiation lengths.

Because the vertex resolution is optimized by choosing a material with short radiation length, BGO was selected. BGO has other advantages: it is mechanically rigid, it emits light of a convenient wavelength (480 nm), and it is an active material. This light may be easily transmitted to a photocathode, through lead-glass light guides.

b. Tracking wire chambers The tracking chamber system is the most crucial component of the NMS because it must provide excellent position resolution for the conversion vertex reconstruction and also handle multiple tracks so as to use the maximum available beam flux. The chambers must have an intrinsic resolution on the order of 100 μm in order to give sub-millimeter vertex resolution. The tracking system found to be capable of providing such resolution was the cathode-strip readout chamber.

The requirements of high resolution and multiple hits per event were achieved by associating two X-Y pairs of anode wire planes and cathode-readout chamber planes with each converter plane. A complete tracking chamber system consists of four pairs of anode/cathode planes. In each pair, the direction of the anode plane is perpendicular to that of the cathode plane. Each anode/cathode pairis separated from the others by a mylar "inactive cathode" plane in order to avoid cross talk between the adjacent pairs.

The active window of the cathode-strip chambers is 35.56 cm × 71.12 cm. This area was determined so that it matched the fiducial area of the NMS calorimeter corresponding to a 4 × 8 array of crystals, thus excluding the crystals along the edges. The total thickness of the chamber system (3.97 cm) was minimized because the acceptance of the spectrometer decreases rapidly with the target-to-detector distance (as R^3). Moreover, the X-Y planes were placed as close as possible to the converter for better position resolution (0.16 cm).

The anode planes are of an alternating-gradient construction: every other wire is a ground wire. The anode wires are gold-plated tungsten 20 μm in diameter, placed 5.556 mm apart, which are run at positive high voltage. Centered between the anode wires are 76-μm, gold-plated, copper-clad, aluminium cathode wires which are run at ground potential [32,33]. Cathode wires are spaced 1.389 mm apart in the cathode plane. Adjacent wires in the cathode plane are connected together to form strips with 2.778-mm separation.

The complete NMS spectrometer with two detectors, two converters per detector, and two X-Y pairs of chambers per converter requires in principle nearly 50,000 channels of amplifiers and ADCs. The number of amplifiers, and therefore of ADCs needed to transmit the pulse information from the wires in the cathode plane, was reduced significantly by multiplexing the cathode channels. This task was accomplished by hard-wiring readout pads together on the chamber before the amplifiers. With these design parameters, there are 32 amplifiers and ADC channels per plane for a total of 512 cathode channels in the complete spectrometer. More details on this multiplexing scheme for cathode-strip readout chambers can be found elsewhere [34].

c. Calorimeter Following the two converter/tracking packages is the calorimeter. Pure CsI was chosen because of its short radiation length (1.85 cm), fast response (more than 50% of the light has a decay time of $\sim$ 20 ns), and reasonable cost. Moreover, it is an absorbing material that is capable of good energy resolution. It is virtually non-hygroscopic, it does not cleave, and it is extremely resistant to radiation damage.

Each calorimeter is composed of a 6×10 array of pure CsI crystals, each of which is optically isolated from its neighbors and coupled to a photomultiplier tube. The 60 crystals are assembled so that the array is a mechanically rigid device which can be deployed in various spatial orientations. The length of each crystal is 30.48 cm so that 97% of photons, having an energy up to 800 MeV, can be detected. The dimensions of the back face of each crystal are 10.16 cm × 10.16 cm. Each crystal is tapered on two sides by 1°, thus making the front-face dimensions 10.16 cm × 9.096 cm. The stability of this arched configuration prevents any possibility of a load being applied to the entrance window of the calorimeter. More than 97% of the deposited energy is contained in a 3×3 cluster of crystals for γ-rays incident at the center of the central crystal in the cluster. The signals of all photomultiplier tubes are summed to give a measure of the total energy of the photon.

2. *Concept of π° detection*

The NMS measures six quantities: the polar and azimuthal angles (θ_1, θ_2, ϕ_1, ϕ_2) and the energies (E_1, E_2) of the two gamma rays from this π^0 decay mode. Under these conditions, a good π° energy resolution can be achieved by measuring precisely the angles of the two photons even with a rough measurement of their energies. The total energy E_{π° and the laboratory scattering angle θ_{π° of a neutral meson are reconstructed in terms of these measured quantities, as shown below.

Considering the decay of the π° with four-momentum p_{π° into two photons (p_1 and p_2), energy and momentum conservation lead to the result that the total π^0 energy is

$$E_{\pi^\circ} = E_1 + E_2 = m_{\pi^\circ} c^2 \sqrt{\frac{2}{(1 - X^2)(1 - \cos\eta)}}\,, \tag{2.3}$$

where the energy sharing parameter between the two photons is

$$X = \frac{E_1 - E_2}{E_1 + E_2}\,, \tag{2.4}$$

and η is the opening angle between the two decay photons in the laboratory frame.

In a similar way, the scattering angle is given by

$$\cos\theta_{\pi^\circ} = \frac{E_1 \cos\theta_1 + E_2 \cos\theta_2}{\sqrt{E_1^2 + E_2^2 + 2E_1E_2\cos\eta}}\,. \tag{2.5}$$

The opening angle η can be determined very precisely by means of tracking chambers. The photon energies E_1 and E_2 are measured with the calorimeters.

In the case of symmetric decays ($E_1 \simeq E_2 \simeq E_{\pi^\circ}/2$; $X \simeq 0$), the π° energy resolution depends almost entirely on the measurement of η. In that case, the measurement of E_1 and E_2 is needed only for the selection of the events within the part of phase space with small X.

III. ANALYSIS

A. Calibration of NMS

Before taking data for the reaction $\pi^- \vec{p} \rightarrow \pi^0 n$, runs of cosmic rays were taken in order to balance the high voltages and to match the hardware gains of the CsI and the BGO crystals. The high voltage for each crystal was adjusted so that the ADC channel number was ten times the expected energy loss in MeV of the cosmic-ray muons. The hardware gains were set such that the energy deposited over all the crystals was uniform. With the detectors oriented with their long axes vertical and the crystals horizontal, events that fired at least five CsI crystals in a vertical column, without firing any CsI crystals in the adjacent columns, were considered CsI cosmic-ray events. During data acquisition, cosmic-ray data were recorded between beam gates along with the data from the π° decay. These cosmic-ray events were used during replay to determine any gain shifts of the crystals during the experiment, and to correct for them. The centroids of cosmic-ray events for the CsI crystals can be determined to about 300 keV, and those for the BGO crystals to about 100 keV, if there are no significant backgrounds.

The second part of the calibration process was a π–stop measurement. A π^- beam was stopped in a pure hydrogen target so as to provide monoenergetic 129.4-MeV photons from the $\pi^-_{\text{stopped}} p \rightarrow \gamma n$ reaction. The data could then be used to optimize the software gains in order to achieve a high resolution. The beam channel was tuned to produce a π^- beam of 54 MeV. The target was a bottle of pure hydrogen gas with a 5.1-cm-thick beryllium absorber placed on the outside of the bottle in order to stop the π^- beam within the gas.

A good calibration is necessary to obtain data with good resolution, because even small relative gain changes can have a large effect on the π° mass reconstruction. A typical invariant π° mass reconstruction is shown in Fig. 5. This quantity is computed in the analyzer according to Eq. (2.3), with $E_1 + E_2$ given by the sum of the energies from the BGO and CsI crystals.

B. Good π° Event

Several tests are necessary to ensure that the data used in the analysis are from good π° events. The first selection of good events is done by the hardware. However, this selection only ensures that the events recorded are coincidence events with the right energy threshold, and that they were not vetoed. Therefore more selections are needed in the software, such as:

1. At least one of the wire chamber systems must fire in each arm of the spectrometer. A chamber system is good when all of the four anode planes fire.
2. The photons from the π° decay must be within the chosen fiducial areas.
3. The photons from the π° decay must be within angular limits which will exclude events that do not come from the target.
4. The events must have an invariant π° mass reconstruction within acceptable resolution limits.

C. Extraction of Asymmetries

1. Definition

The experimental differential cross section is given by

$$\frac{d\sigma}{d\Omega} = \frac{Y\,J}{N_{\pi^-}\,N_p\,\Delta\Omega\,\varepsilon_{WC}\,f_{\gamma\gamma}\,\tau}\,. \tag{3.1}$$

Here, Y is the yield, J the Jacobian of the transformation of cross section from the laboratory to the center-of-mass frame, N_{π^-} the number of π^- particles in the incident beam, N_p the number of protons in the target per cm^2, $\Delta\Omega$ the effective solid angle, ε_{WC} the overall wire chamber efficiency, $f_{\gamma\gamma}$ the $\pi^\circ \rightarrow \gamma\gamma$ branching ratio, and τ the experimental live-time. The analyzing power is given by Eq. (1.4).

When extracting the analyzing power from the data, the yields are used instead of the differential cross sections because quantities such as the absolute beam-flux scale, target thickness, solid angle, and branching ratio will cancel. These factors are assumed to be unchanged between polarization runs and are independent of the scattering angle. Thus, by substituting the yield with the remaining normalization factors into the expression for A_y, one obtains

$$A_y = \frac{Y^n_\uparrow - Y^n_\downarrow}{P_\downarrow Y^n_\uparrow + P_\uparrow Y^n_\downarrow}\,, \tag{3.2}$$

where $Y^n_\uparrow$ ($Y^n_\downarrow$) is the normalized yield for spin–up (spin–down), with backgrounds subtracted. The remaining normalization factor is

$$N = \frac{1}{\Phi_{IC}\,\varepsilon_{WC}\,\tau}\,, \tag{3.3}$$

where Φ_{IC} is the relative pion beam flux, as measured by the ion chamber.

Typical spin–up, spin–down, and background spectra are shown in Fig. 6. The small peak in the background spectrum under the hydrogen peak is due to the ^{3}He in the dilution refrigerator. More details on the background can be found in Sect. III C 4.

2. Adding runs with different polarization

In order to minimize systematic uncertainties between spin–up and spin–down, the target polarization was flipped systematically. Therefore, data from multiple runs, each with a different value of the polarization, must be combined in order to extract the yields of the spin–up, spin–down, and background spectra. For statistical reasons, it is better to sum the events in the spectra (after background subtraction) over all of the runs for a particular kinematic setting and target spin orientation rather than to obtain the yields individually with a peak-fitting program [35]. Summing the events simplifies the problem of adding runs of different target polarizations, and the expression of the analyzing power becomes

$$A_y = \frac{J\sum_i Z^n_{\uparrow i} - I\sum_j Z^n_{\downarrow j}}{\sum_i Z^n_{\uparrow i}\sum_j P_{\downarrow j} + \sum_j Z^n_{\downarrow j}\sum_i P_{\uparrow i} - Bg} \tag{3.4}$$

where

$$Bg = B^n(I\sum_j P_{\downarrow j} + J\sum_i P_{\uparrow i}) \,. \tag{3.5}$$

Here i (j) labels the spin-up (spin-down) runs, I (J) is the total number of runs with spin-up (spin-down), Z^n is the normalized yield of the observed spectra, and B^n is the normalized yield of the background that needs to be subtracted ($Z^n = Y^n + B^n$).

3. "Out-of-plane" correction

Due to the large acceptance area of the NMS spectrometer, the detected π^0's can have scattering planes that are rotated out of the horizontal plane which is perpendicular to the target polarization. These "out-of-plane" events dilute the observed analyzing power because

$$d\sigma_{\uparrow/\downarrow} = d\sigma\left[1 + A_y \mathbf{P}_{\uparrow/\downarrow}\cdot\hat{\mathbf{n}}\right] \,, \tag{3.6}$$

where $d\sigma$ is the differential cross section for an unpolarized target, $\hat{\mathbf{n}}$ is a unit vector normal to the scattering plane, and $\mathbf{P}_i$ is a positive real quantity which has a magnitude equal to the polarization of the target. The angle between the normal to the particle's scattering plane $\hat{\mathbf{n}}$, and the target polarization vector $\mathbf{P}$ is defined by ϕ. The value of $\cos\phi$ for each event is directly extracted from the data during the replay according to

$$\cos\phi = \frac{\sqrt{p^2_{\pi^0,y} + p^2_{\pi^0,z}}}{\sqrt{E_1^2 + E_2^2 + 2E_1E_2\cos\eta}} \,. \tag{3.7}$$

The value of ϕ was less than 10° for every kinematic set.

Correcting for the effects of the "out-of-plane" angles, the linear combination of sums of yields over all runs and all events for spin–up and spin–down gives

$$A_y = \frac{JJ'\sum_i Z^n_{\uparrow i} - II'\sum_j Z^n_{\downarrow j}}{\sum_i Z^n_{\uparrow i}\sum_j P_{\downarrow j}\sum_{j'}\cos\phi_{jj'} + \sum_j Z^n_{\uparrow j}\sum_i P_{\downarrow i}\sum_{i'}\cos\phi_{ii'} - Bgd} \,, \tag{3.8}$$

where

$$Bgd = B^n(II'\sum_j P_{\downarrow j}\sum_{j'}\cos\phi_{jj'} + JJ'\sum_i P_{\uparrow i}\sum_{i'}\cos\phi_{ii'}) \,. \tag{3.9}$$

The symbols are the same as for Eq. 3.4 with the addition that i' (j') labels the events within runs i (j), and I' (J') is the total number of events with spin-up (spin-down). The polarizations were not corrected on an event-by-event basis, but scaled by the sum of the $\cos\phi$ values for all of the events in the run.

4. Background subtraction

For the method of summing to be consistent, it is required to have a good background subtraction and to know the boundaries of the "pure" hydrogen peak. The analyzing powers are very sensitive to the quality of background subtraction, and an inexact subtraction could introduce a false asymmetry.

Ideally, background data would be taken with the complete target but with the polarizable hydrogen removed. However, even if a strong effort were made to build a background target as identical as possible to a butanol target without hydrogen, as explained in Sect. II B 4, some discrepancies still exist. It is not possible to create a target with the correct molecular combination of (C_4O), or even with pure carbon or oxygen at the same density as the one in the butanol target. From Tables I and II, it is clear that the effective thicknesses of the elements in both targets are not exactly identical. Moreover, the background target is half the physical thickness of the butanol target (see Sect. II B 4), which increases the quantity of ^{3}He in the path of the incident pion beam (see Fig. 3). These discrepancies

are listed in Table III. Nevertheless, it is safe to assume that the background due to the dilution refrigerator itself is perfectly subtracted because the background target and the butanol target were both enclosed within the same refrigerator.

In the case of perfect background subtraction, one would expect the analyzing power to be constant within the hydrogen peak and to be zero outside it, as illustrated in Fig. 7. When the analyzing powers were plotted for each missing-mass channel, it was obvious that the background was not uniform in the tails of the hydrogen peak, as shown in Fig. 8. However, it can be seen that within the interval $[Q_1, Q_2]$, the analyzing power is constant. This interval corresponds to the hydrogen peak. Therefore a cut on the missing mass was made in order to suppress the events that could create a false asymmetry. Only the data within the interval $[Q_1, Q_2]$ were kept. This method was applied to each angular bin of the kinematic sets because the positions of the ^{3}He, C, and O peaks in the missing-mass spectra are strongly dependent on the beam momentum and the scattering angle.

D. Uncertainties in A_y

The values of the statistical uncertainties for the non-normalized yield of the observed spectra were evaluated by using Gaussian statistics, $\sigma_{Z_{\uparrow/\downarrow}} = \sqrt{Z_{\uparrow/\downarrow}}$. The polarization direction was flipped systematically for each kinematic set in order to minimize systematic uncertainties. The sequence used was $\uparrow\downarrow\downarrow\uparrow$ with some background runs inserted. In practice, multiple data runs, each of about two hours duration, were taken for each spin orientation. The procedure allows a cross-check of the yields by calculating the analyzing powers for random combinations of similar spin–up or spin–down runs. From these results, which ideally would have $A_y = 0$, it was possible to determine which combinations were inconsistent with the expected value and then to infer those runs that were responsible for any inconsistency. Some inconsistencies arose, for example, from computer failures before the end of a run, or failures of the wire-chamber high voltage system. Some of these issues could be resolved from the remaining data for a run.

Once the inconsistencies were removed, the set of analyzing powers A_i for random combinations of runs with identical spin orientation were extracted, as illustrated in Fig. 9. The standard deviation for this distribution, which measures the fluctuations of A_i about zero, is $\sigma_{A_i} = 0.031$. The variations of these analyzing powers can arise from fluctuations in the scaler counters, fluctuations in the steering of the beam, and uncertainties in the determination of the target polarization. If the fluctuations of the analyzing powers A_i about zero were due only to statistical uncertainties, one would expect that the standard deviation of the distribution $A_i/\Delta A_i$ to be equal to unity, i.e.

$$\sigma = \sqrt{\frac{1}{N-1}\sum_i \left(\frac{A_i}{\Delta A_i} - \mu\right)^2} = 1 = \sigma^{\mathrm{stat}} , \tag{3.10}$$

where N is the total number of random combinations, the A_i are the analyzing-power values of each combination, and the mean μ is given by

$$\mu = \frac{1}{N}\sum_i \frac{A_i}{\Delta A_i} . \tag{3.11}$$

However, the standard deviation obtained for the distribution is $\sigma = 1.65$. It represents the fluctuations due to both statistics and systematics. Therefore, with the assumption that the errors combine in quadrature, the standard deviation for the systematic error is $\sigma^{\mathrm{syst}} = \sqrt{1.65^2 - 1^2} = 1.31$. Converting back to the A_i distribution, the standard deviation due to the systematic uncertainties is

$$\sigma_{A_i}^{\mathrm{syst}} = \frac{\sigma^{\mathrm{syst}}\,\sigma_{A_i}}{\sigma} = 0.025 . \tag{3.12}$$

Therefore, the "total" uncertainty for the experimental analyzing powers

$$\sigma_{A_y} = \sqrt{(\sigma_{A_y}^{stat})^2 + (\sigma_{A_y}^{syst})^2} \tag{3.13}$$

includes the statistical errors and an empirical estimate of the systematic errors.

The overall polarization uncertainty only includes the systematic errors because the statistical errors are very small. The primary sources of the polarization error arise from the accuracy of the temperature measurements for the thermal-equilibrium data, and the ability to fit the spectra for the enhanced-polarization measurements. The overall polarization uncertainty was estimated to be 4.5% [25].

IV. RESULTS

A. Pion beam energy and scattering angle

The energy and direction of the beam at the interaction vertex must be evaluated in order to determine the energy of the reaction and the scattering angles in the final tabulations, and for use in the replay of the data.

The energy loss of the pion was evaluated for all materials between the exit window of the channel and the butanol target, including kapton at the end of the beam pipe, the ion chamber, air volume between the ion chamber and the refrigerator, and all refrigerator and target materials. About 95% of the energy loss occurred in the cryostat. The energy-loss calculations were based on the expressions of Barkas and Berger [36].

As mentioned earlier in Sect. II A, the pion beam deviates from the direct beam line because of the magnetic field for the polarized target. However the beam was suitably steered by the magnet Werbecka so that it passed through the target at the center of the magnetic field. Therefore the effect of the Werbecka magnet and the magnetic field of the target gives a 0° exit angle different from the standard 0° beam line (see Fig. 2). The accurate determination of the angle θ_{exit} (θ in Fig. 2) between the new and the standard 0° exit angle is very important for determinating the scattering angle θ_{scat}. Calculations of θ_{exit} with different algorithms from maps of the Zoltan magnetic field profile agreed to better than 0.1°.

In order to determine the scattering angles, the positions of the two detectors also need to be known accurately. These positions were determined from theodolite measurements. Estimates of the uncertainties of the scattering angles are more difficult to make, but they are unlikely to exceed 0.5°.

B. Consistency checks

1. Fiducial areas

As mentioned previously, the NMS detectors were designed and built for a main fiducial area of 4 × 8 CsI crystals. It is also possible to choose smaller fiducial areas as determined by a given number of radiation lengths into the 4 × 8 group. The fiducial area used for this spectrometer followed a conic projection back to the target. The main requirement in the selection of the fiducial area is that the limits must be sufficiently far from the edges of the wire-chamber planes because events near the edges could produce showers that might exit the chamber window, resulting in too low an energy.

The check for consistency was to define different fiducial areas in the BGO planes and to require that the two decay photons fall within these windows. During replay, analyzing powers were calculated for different fiducial areas. It was found that the analyzing powers were independent of the chosen fiducial area, as expected, which proved their consistency even within the small statistical error bars.

2. CsI crystal temperature

The CsI crystals and/or the phototubes are known to be very sensitive to temperature. To prevent any effects from variations of the ambient temperature, a cooling system was installed on the detectors. The gains of the CsI crystals are inversely correlated with the detector temperature and therefore to the room temperature. The centroids of the energy distributions of cosmic-ray events are a sensitive measure of the CsI crystal gains. These centroids were plotted with respect to time and they showed that any effects from ambient temperature variations on the detector temperatures and the CsI gains were very small and well within the uncertainties from other sources.

3. Overall wire chamber efficiency and live-time

The overall wire-chamber efficiency and the live-time variables have a direct impact on the analyzing power through the normalization factor. These two parameters were evaluated and plotted for every run. Both the overall wire-chamber efficiency and the live-time were very stable within most of the kinematic sets. However, in some cases, the live-time changed by more than 1% from one polarization direction to the other, hence the importance of including it in the normalization factor. The overall wire-chamber efficiencies differed by well less than 0.5%, typically less than 0.1%, from one polarization direction to the other, which shows the high stability of the NMS over the course of this experiment ($\sim$ 2 months).

C. Determination of the Angular Bins

The NMS angular coverage was approximately 20°. For better angular resolution, the data were divided into three angular bins during replay. The boundaries of each angular bin were determined as follows:

1. A cut was applied on the missing mass in order to reject the events due to background.
2. The number of events left in the missing-mass spectrum was extracted.
3. The histogram of the scattering angle was then divided into three bins, determined so that there would be approximately equal statistics in each bin.

The scattering angle for each angular bin is the weighted average of the scattering angles for each event within the cut imposed on the missing mass. A simple average between the minimum and maximum values of the scattering angle would be wrong due to the non-uniform distribution of events in the scattering-angle distribution.

D. Results

The results from the analysis of the data are shown in Fig. 10 with the VPI SM95 [5] and Karlsruhe-Helsinki KH80 [37,38] phase shift solutions superimposed. The error bars are only statistical. The analyzing powers are plotted against the center-of-mass scattering angles for each of the four energies. The data for several sets of very similar angles were taken with adjacent and overlapping kinematic positionings of the NMS. It is important to note the good agreement of the data values for these sets. The data for these plots are given in Table IV, along with their respective statistical and systematic errors. However, the overall polarization uncertainty of 4.5% is omitted because the analyzing-power values scale with a shift in polarization values.

V. DISCUSSION

High quality analyzing powers for the $\pi^- \vec{p} \to \pi^0 n$ reaction have been measured over a broad angular range at incident kinetic energies of 98.1, 138.8, 165.9, and 214.4 MeV. The main goal of experiment E1178 was to provide new, high-precision polarization data to the πN SCX database. Only 38 analyzing-power measurements existed before this experiment for energies ranging from 10 to 230 MeV (see Table V). Experiment E1178 nearly doubled the existing database with its new 36 analyzing powers. Therefore, an important gap in polarization observables for the SCX channel has been filled.

The data are well described by the SM95 solution of the VPI phase-shift analysis [5]. In principle, the final A_y results can be combined with cross-section measurements from the $\pi^- p \to \pi^0 n$ reaction to form spin-up and spin-down "transversity" cross sections [41]. These cross sections are defined by the relations

$$d\Sigma_\uparrow = d\sigma(1 + A_y) \tag{5.1}$$

$$d\Sigma_\downarrow = d\sigma(1 - A_y)\,. \tag{5.2}$$

As a result of the triangular inequality relationships arising from isospin invariance in the πN system, the transversity cross sections must be within limits given by combinations of the amplitudes from the $\pi^+ p$ and $\pi^- p$ elastic-scattering reactions. Thus,

$$\frac{1}{2}\left(\sqrt{d\Sigma^+_\uparrow} - \sqrt{d\Sigma^-_\uparrow}\right)^2 \le d\Sigma^0_\uparrow \le \frac{1}{2}\left(\sqrt{d\Sigma^+_\uparrow} + \sqrt{d\Sigma^-_\uparrow}\right)^2\,, \tag{5.3}$$

where $d\Sigma^+ = d\Sigma(\pi^+ p \to \pi^+ p)$, $d\Sigma^- = d\Sigma(\pi^- p \to \pi^- p)$, and $d\Sigma^0 = d\Sigma(\pi^- p \to \pi^0 n)$, with a similar expression for spin down.

Because the region of the $\Delta(1232)$ is dominated by a single resonance, the SCX transversity cross sections are expected to lie very close to the lower limit of the elastic-scattering combination. This situation is ideal for investigating isospin breaking in the πN system. Even relatively small isospin breaking might push the transversity cross sections significantly outside the good-isospin limits. Unfortunately, however, SCX cross-section data of sufficient accuracy are not currently available for such a test. Hope is expressed that this situation can be remedied soon. It is very important to know whether the unusually large isospin breaking that has been observed at pion energies below 100 MeV [7,10] also extends into the $\Delta(1232)$ region. A solid understanding of such possible isospin breaking is essential in order to refine the extraction of the important $\Sigma_{\pi N}$ term.

VI. ACKNOWLEDGEMENTS

The authors wish to thank the management of LAMPF for coordinating resources for this experiment at a difficult time and for ensuring that it could be completed. The accelerator and the technical staff provided outstanding support for the preparation and execution of the experiment. Special thanks are also extended to John Zumbro for expert assistance with the surveys, and to John O'Donnell for very helpful assistance in the analysis of the data. This work was supported in part by the National Science Foundation under grants PHY92-000435 and PHY95-04847; the U.S. Department of Energy, Division of Nuclear Physics under grants W-31-109-ENG-38, DE-FG03-94ER40860, DE-FG03-94ER40847 and others; and the German Bundesministerium für Bildung and Forschung (BMFT) under grant 06Tue669.

---

* Present address: INFN-Laboratori Nazionali di Frascati, Via Enrico Fermi 40, 00044 Frascati, Italy.
† Present address: Department of Physics and Astronomy, University of Montana, Missoula, Montana 59812, USA.
‡ Present address: Data Ventures, Los Alamos, NM 87544, USA.
§ Present address: Department of Physics, University of Texas at El Paso, El Paso, Texas 79968-0515, USA.
‖ Present address: Los Alamos National Laboratory, Los Alamos, NM 87545, USA.
¶ Present address: Department of Radiation Oncology, University of Michigan Medical Center, Ann Arbor, MI 48109, USA.

[1] R. Koch and E. Pietarinen, Nucl. Phys. A **448**, 707 (1986).
[2] V. Stocks, R. Timmermans, and J. J. de Swart, Phys. Rev. C **47**, 512 (1993).
[3] V. G. J. Stokes *et al.*, Phys. Rev. Lett. **61**, 1702 (1988).
[4] J. R. Bergervoet *et al.*, Phys. Rev. C **41**, 1435 (1990).
[5] R. A. Arndt *al.*, Phys. Rev. C **52**, 2120 (1995).
[6] R. G. E Timmermans, in *πN Newsletter* No. **13**, Vancouver, 80 (1997).
[7] W. R. Gibbs, L. Ai, and W. B. Kaufmann, Phys. Rev. Lett. **74**, 3740 (1995); Phys. Rev. C **57**, 784 (1998).
[8] T. E. O. Ericson *et al.*, Phys. Rev. Lett. **75**, 1046 (1995).
[9] T. E. O. Ericson and B. Loiseau, Phys. Lett. B **393**, 167 (1997).
[10] E. Matsinos, Phys. Rev. C **56**, 3014 (1997).
[11] J. Gasser and H. Leutwyler, Phys. Rep. **C87**, 77 (1982).
[12] J. Gasser, H. Leutwyler, and M. E. Sainio, Phys. Lett. B **253**, 252 (1991), and references therein.
[13] S. Weinberg, in *A Festschrift for I. I. Rabi*, N.Y. Acad. Sci. **38**, 185 (1977). S. Weinberg in *Chiral Dynamics: Theory and Experiment*, A. M. Bernstein and B. R. Holstein, eds. (Springer Verlag, Berlin, 1995).
[14] M. E. Sevior *et al.*, Phys. Rev. C **40**, 2780 (1989).
[15] G. J. Hofman, Ph. D. Dissertation, The University of British Columbia (1997).
[16] Proposal for a High Resolution Spectrometer for Neutral Mesons, R.L. Boudrie, J.L. Matthews, and C.L. Morris, Los Alamos National Laboratory Report No. LA-UR-91-1847, 1991.
[17] R. L. Burman, R. L. Fulton and M. Jackobson, Nucl. Instrum. Methods **131**, 29 (1975).
[18] R. L. Fulton, Mechanical Design of the LAMPF Low-Energy Pion Channel, Los Alamos National Laboratory Report No. LA-5222-MS, 1973.
[19] K. L. Brown *et al.*, computer code TRANSPORT, CERN 80-04, Geneva, 1980.
[20] A. Abragam and M. Goldman, *Nuclear Magnetism: Order and Disorder* (Oxford University Press, Oxford, 1982).
[21] C. D. Jeffries, *Dynamic Nuclear Orientation* (Interscience Publishers, New York, 1963).
[22] C. P. Slichter, *Principles of Magnetic Resonance* (Springer-Verlag, New York, 1990).
[23] D. G. Crabb and W. Meyer, Annu. Rev. Nucl. Part. Sci. **47**, 67 (1997).
[24] R. Court *et al.*, Nucl. Instrum. Methods **A324**, 433 (1993).
[25] S. I. Penttilä *et al.*, *Proceedings of the Workshop on NMR in Polarized Targets*, Charlottesville, VA, April 1998 (in press).
[26] H. London and G. R. Clarke, Phys. Rev. **128**, 1992 (1962).
[27] T. O. Niinikoski and F. Udo, Nucl. Instrum. Methods **134**, 219 (1976).
[28] T. O. Niinikoski and J.-M. Rieubland, *Proceedings of the International Cryogenic Engineering Conference*, (Butterworth, Guildford, 1982), p. 580.
[29] S. Mango, Ö. Runólfsson and M. Borghini, Nucl. Instrum. Methods **72**, 45 (1969).
[30] M. Krumpolc and J. Roček, J. Am. Chem. Soc. **101**, 3206 (1979).
[31] Particle Data Group, Eur. Phys. J. C **3**, 1 (1998).
[32] G. Charpak, D. Rahm and H. Steiner, Nucl. Instrum. Methods **80**, 13 (1970).
[33] A.H. Walenta, J. Heinz and B. Schurlein, Nucl. Instrum. Methods **93**, 373 (1971).

[34] M. W. Rawool-Sullivan *et al.*, Nucl. Instrum. Methods **A311**, 168 (1992).
[35] P. R. Bevington, *Data Reduction and Error Analysis for the Physical Sciences* (McGraw-Hill, Inc., New York, 1992).
[36] W. H. Barkas and M. J. Berger, Tables of energy losses and ranges of heavy charged particles, Technical Report No. SP 3013, NASA, 1964.
[37] G. Höhler, in *Landolt-Börnstein* Vol. **I/9b2**, edited by H.Schopper, (Springer-Verlag, 1983).
[38] R. Koch and E. Pietarinen, Nucl. Phys. **A336**, 331 (1980).
[39] J. C. Staško, Ph. D. thesis, University of New Mexico, 1993; B. Bassaleck *et al.*, in πN *Newsletter* No. **8**, Vol I, Boulder, 150 (1993).
[40] J. J. Görgen *et al.*, Phys.Rev. D **42**, 2374 (1990).
[41] G. J. Kim *et al.*, Phys. Rev. D **41**, 733 (1990).

FIG. 1. Floor layout of the experiment in the LEP channel. Each crate, which is a detector arm of the NMS, can be rotated independently around the target.

FIG. 2. Schematic layout of the extended LEP beam line. The upper boxes represent the channel exit and quadrupole magnets. Pion trajectories are bent by the magnetic fields of Werbecka and Zoltan (not to scale).

FIG. 3. The polarized and background targets in the mixing chamber of the dilution refrigerator between the poles of Zoltan magnet (vertical slice through the center of the cryostat and magnet.)

FIG. 4. Schematic diagram of the Neutral Meson Spectrometer. The photons in each detector are detected by two planes of active BGO converters and tracking chambers followed by a total-energy calorimeter.

FIG. 5. Invariant π^0 mass reconstruction.

FIG. 6. Spin–up, spin–down, and background spectra as a function of the missing mass (relative to the neutron mass) at several different center-of-mass scattering angles $\theta_{c.m.}$ at 138.8 MeV. The spectrum with higher counts is the spin–up spectrum.

FIG. 7. Constant analyzing power within the interval $[Q_1, Q_2]$ for perfect background subtraction.

FIG. 8. A representative spectral distribution of experimental analyzing powers for each missing-mass channel.

FIG. 9. Analyzing powers for combinations of runs with the same kinematic conditions and spin direction. The error bars represent the statistical uncertainties.

FIG. 10. Analyzing powers for $\pi^- \vec{p} \rightarrow \pi^0 n$ at $T_{\pi^-} = 98.1$, 138.8, 165.9, and 214.4 MeV. The solid lines are the SM95 phase shift solutions of the VPI group and the dashed lines the KH80 ones. The error bars are only statistical, and do not include the target polarization uncertainty of 4.5%.

TABLE I. Effective thickness of the butanol target chemical components.

Element	Mass Fraction (%)	Effective Thickness (g/cm^2)
H	12.92	0.107
C	61.57	0.487
O	24.95	0.197

TABLE II. Effective thickness of the background target chemical component.

Element	Mass Fraction (%)	Effective Thickness (g/cm^2)
C	74.03	0.518
O	25.97	0.172

TABLE III. Background discrepancies.

Element	Effective Thickness (g/cm^2)		$\frac{\text{Backgd}-\text{Butan}}{\text{Backgd}}$ (%)
	Background Target	Butanol Target	
^{3}He	0.187	0.149	+20
C	0.518	0.487	+6
O	0.172	0.197	−14.5

TABLE IV. Analyzing powers at 98.1, 138.8, 165.9 and 214.4 MeV. The total uncertainty σ_{A_y} is defined in Sect. III D. The errors do not include the overall target polarization uncertainty of 4.5%.

T_{π^-} (MeV)	Scattering Angle c.m. (deg)	lab (deg)	A_y	$\sigma_{A_y}^{stat}$	σ_{A_y}
98.1	8.02	6.51	0.054	0.019	0.031
	16.61	13.51	0.108	0.022	0.033
	28.06	22.91	0.223	0.021	0.033
	54.12	44.92	0.491	0.019	0.031
	71.90	60.70	0.499	0.019	0.031
	86.05	73.89	0.349	0.021	0.033
138.8	10.87	8.59	0.076	0.024	0.035
	20.00	15.84	0.169	0.025	0.035
	28.60	22.72	0.200	0.013	0.028
	30.94	24.61	0.231	0.016	0.030
	41.94	33.59	0.314	0.015	0.029
	51.19	41.31	0.426	0.021	0.033
	55.06	44.59	0.450	0.021	0.033
	65.89	53.97	0.556	0.019	0.031
	78.64	65.42	0.5545	0.031	0.040
	78.76	65.54	0.553	0.026	0.036
	91.81	77.85	0.428	0.025	0.035
	103.05	89.00	0.3125	0.027	0.037
165.9	14.13	10.97	0.109	0.014	0.029
	24.90	19.41	0.187	0.015	0.029
	29.04	22.68	0.193	0.013	0.028
	36.38	28.54	0.285	0.016	0.030
	41.86	32.97	0.322	0.013	0.028
	53.99	42.98	0.423	0.016	0.030
	56.59	45.17	0.461	0.013	0.028
	69.95	56.70	0.681	0.018	0.031
	79.10	64.93	0.708	0.038	0.045
	82.41	67.97	0.664	0.019	0.031
	91.95	77.00	0.639	0.031	0.040
	102.52	87.45	0.454	0.027	0.037
214.4	21.91	16.55	0.150	0.012	0.028
	32.60	24.77	0.248	0.014	0.029
	42.82	32.80	0.326	0.018	0.031
	49.62	38.25	0.4315	0.014	0.029
	61.27	47.85	0.5595	0.020	0.032
	73.32	57.34	0.663	0.022	0.032

TABLE V. Analyzing-power database for πN charge-exchange below 230 MeV prior to this experiment.

T_{π^-} (MeV)	Angular range θ_{cm} (deg)	Number of Points	Author
100.00	75.00 - 130.00	4	Staško [39]
150.00	35.00 - 141.00	8	Staško [39]
161.00	28.13 - 73.08	8	Görgen [40]
192.20	32.50 - 89.30	5	Kim [41]
200.00	35.00 - 141.00	8	Staško [39]
205.90	30.80 - 87.60	5	Kim [41]

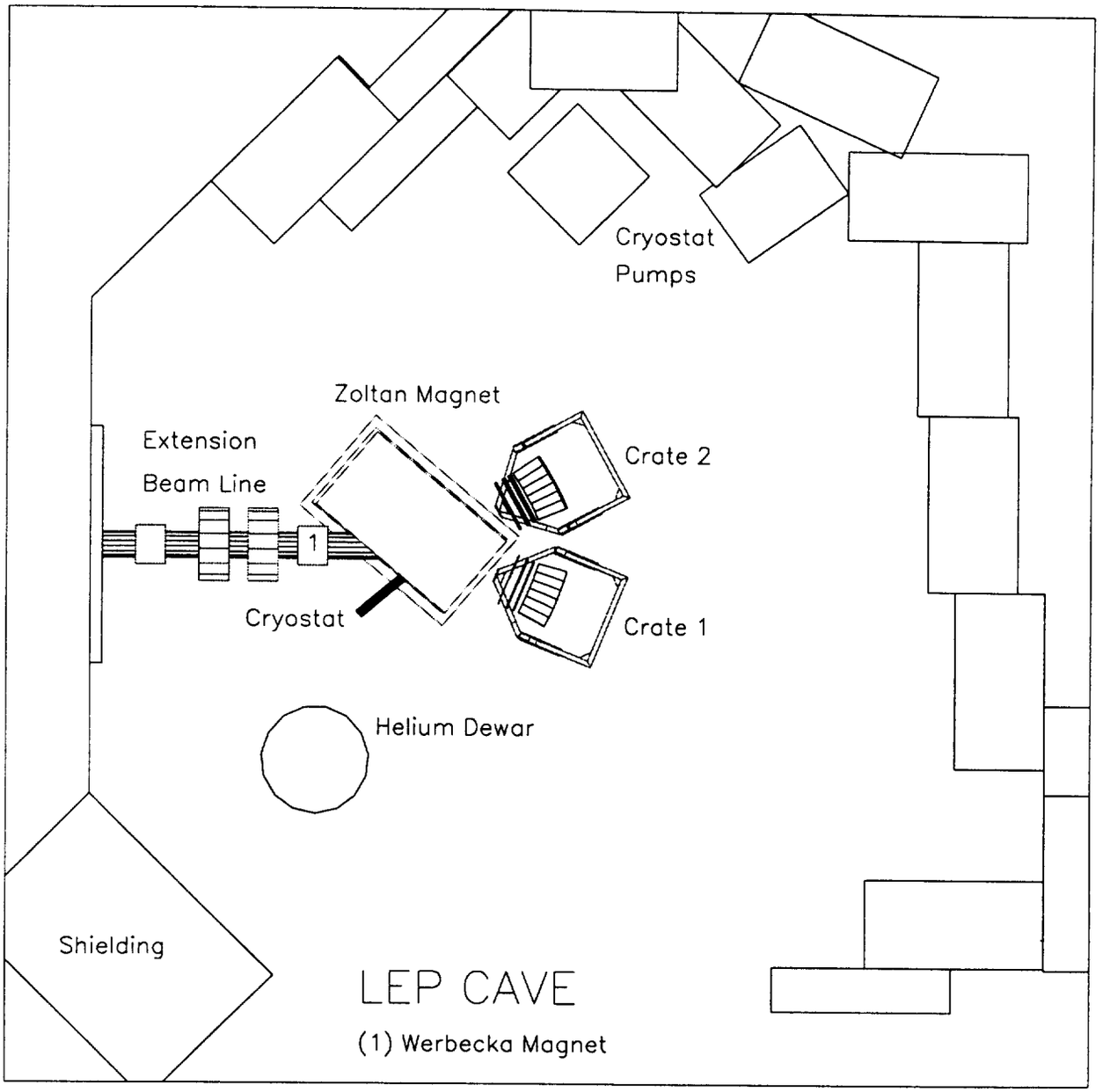

FIG. 1. Gaulard, "Analyzing powers..."; PRC

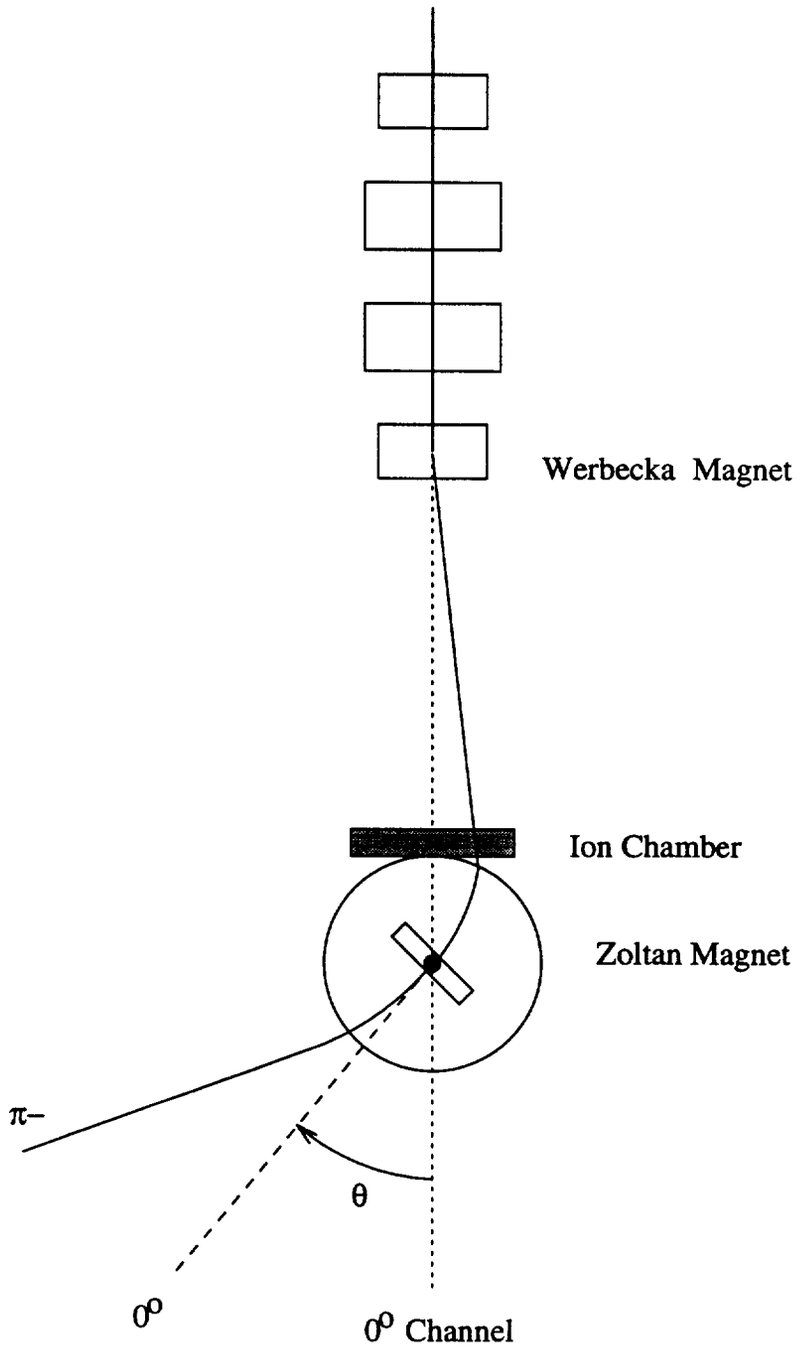

FIG. 2. Gaulard, "Analyzing powers..."; PRC

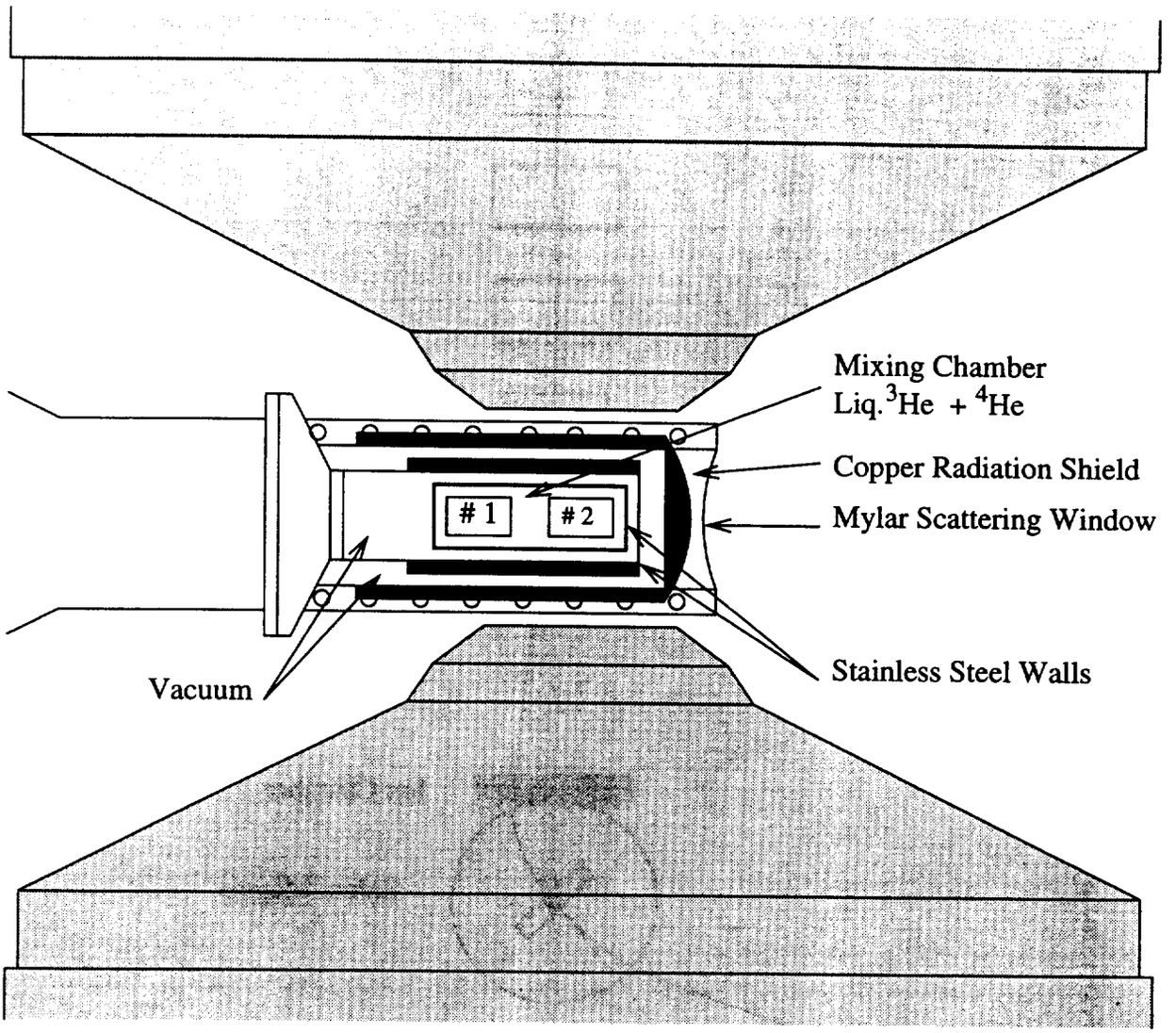

1 Background Target

2 Polarized Target

Poles of Zoltan Magnet

FIG. 3. Gaulard, "Analyzing powers..."; PRC

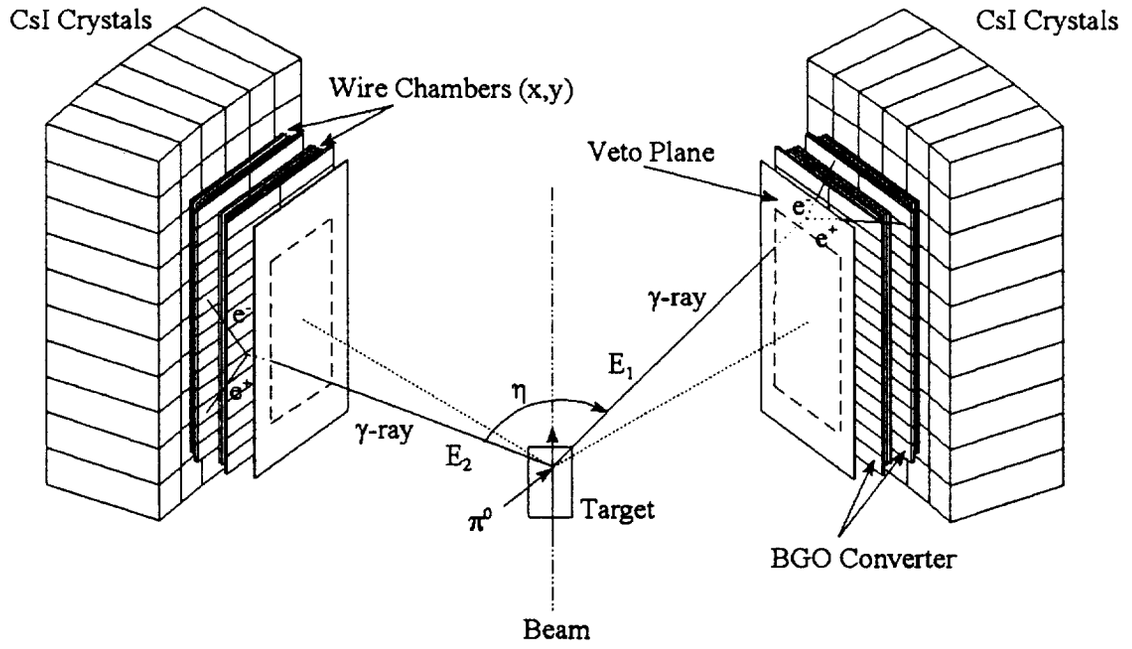

FIG. 4. Gaulard, "Analyzing powers..."; PRC

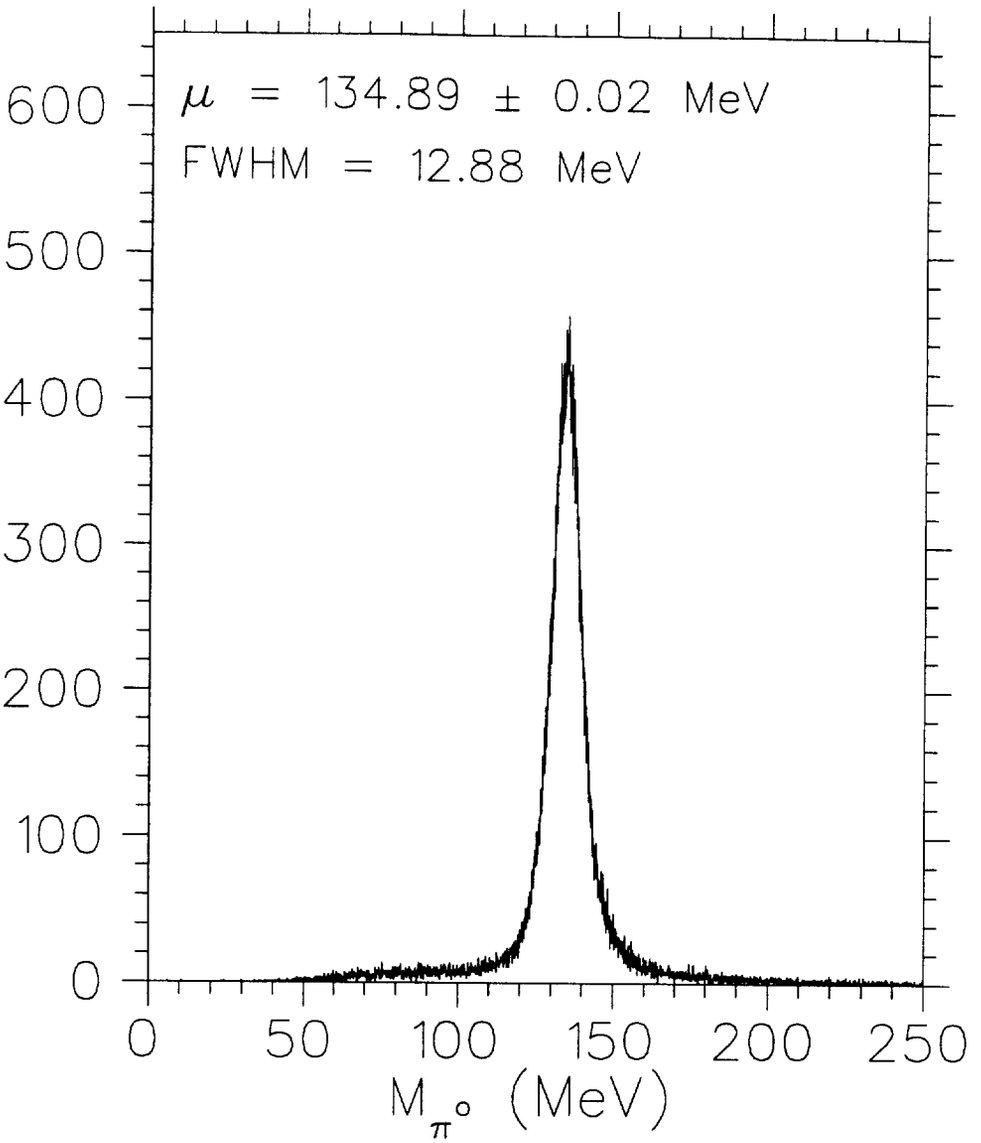

FIG. 5. Gaulard, "Analyzing powers..."; PRC

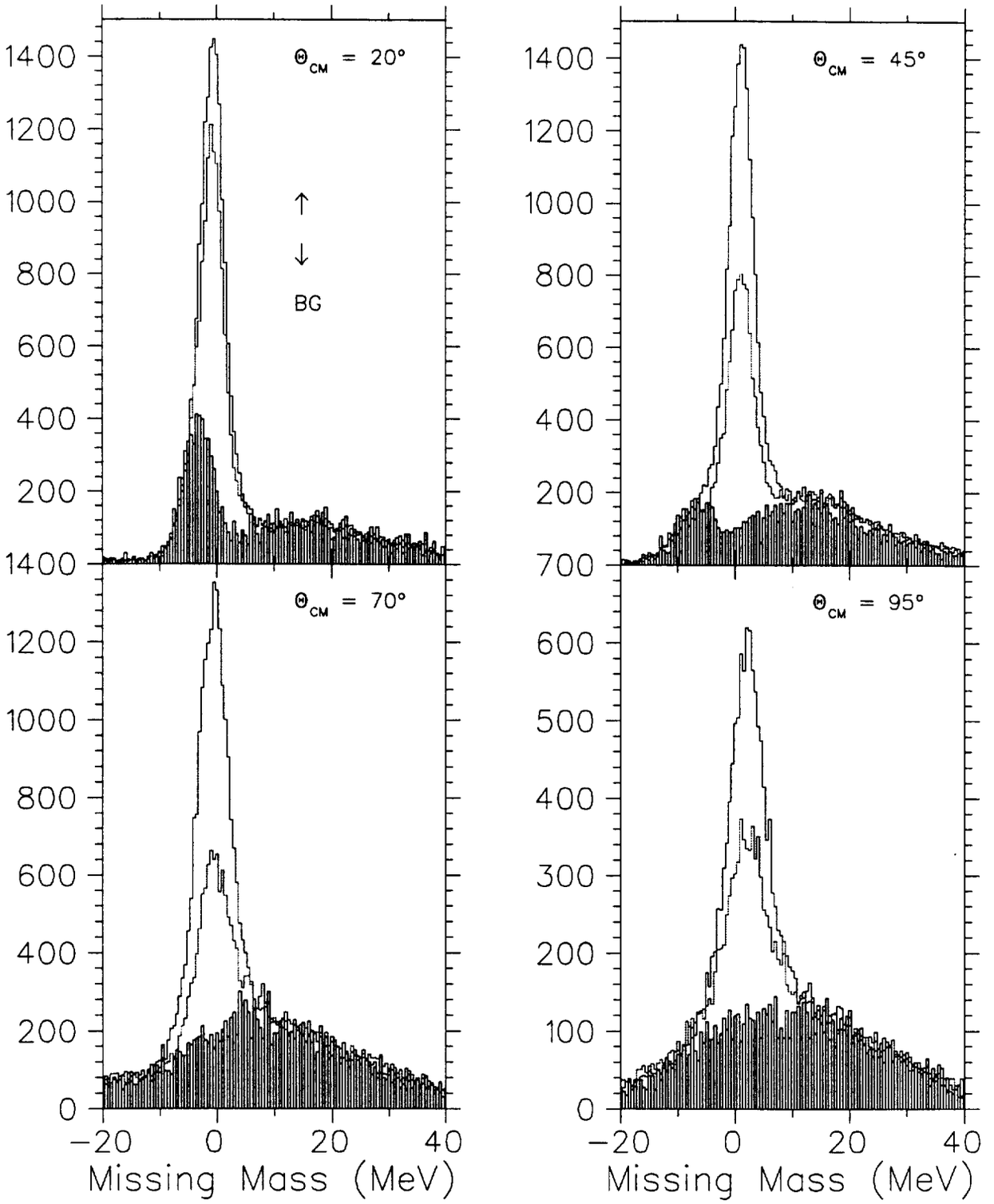

FIG. 6. Gaulard, "Analyzing powers..."; PRC

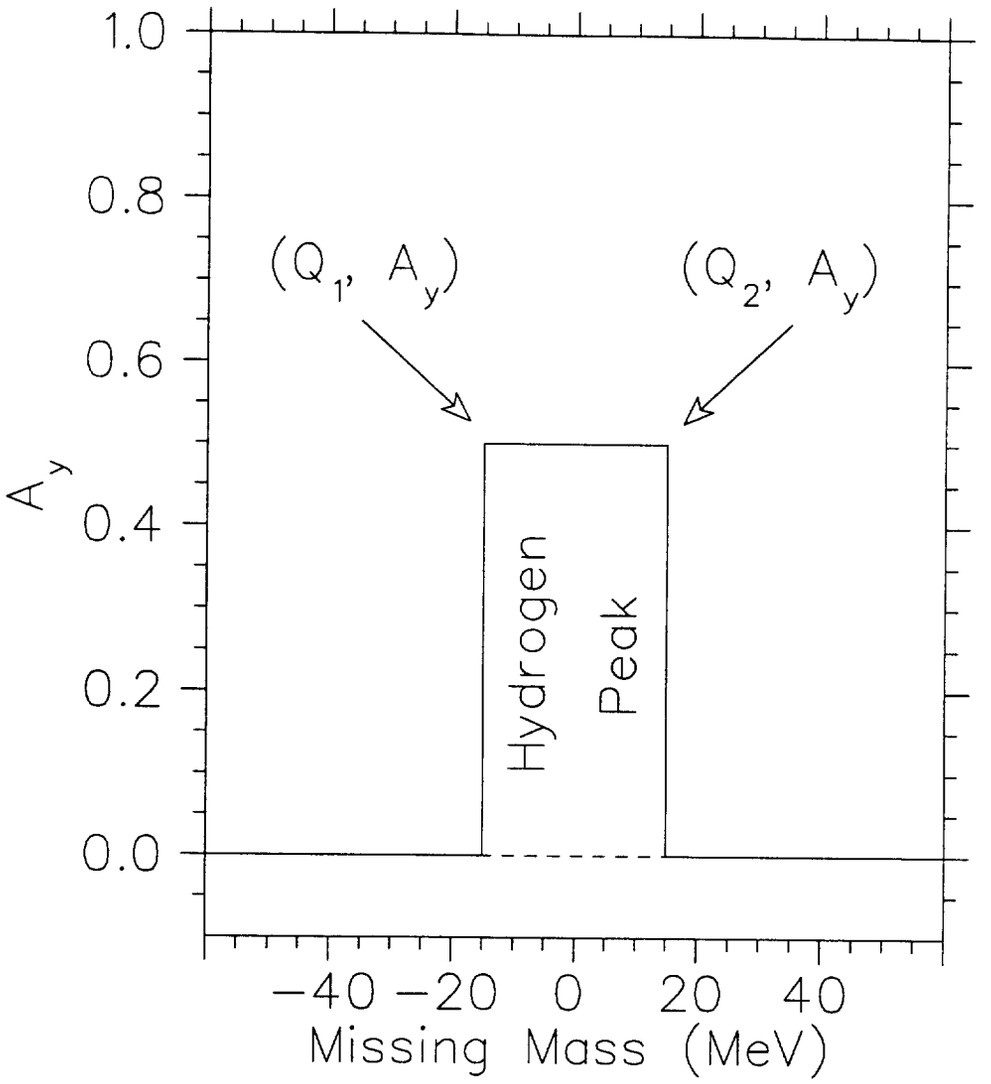

FIG. 7. Gaulard, "Analyzing powers..."; PRC

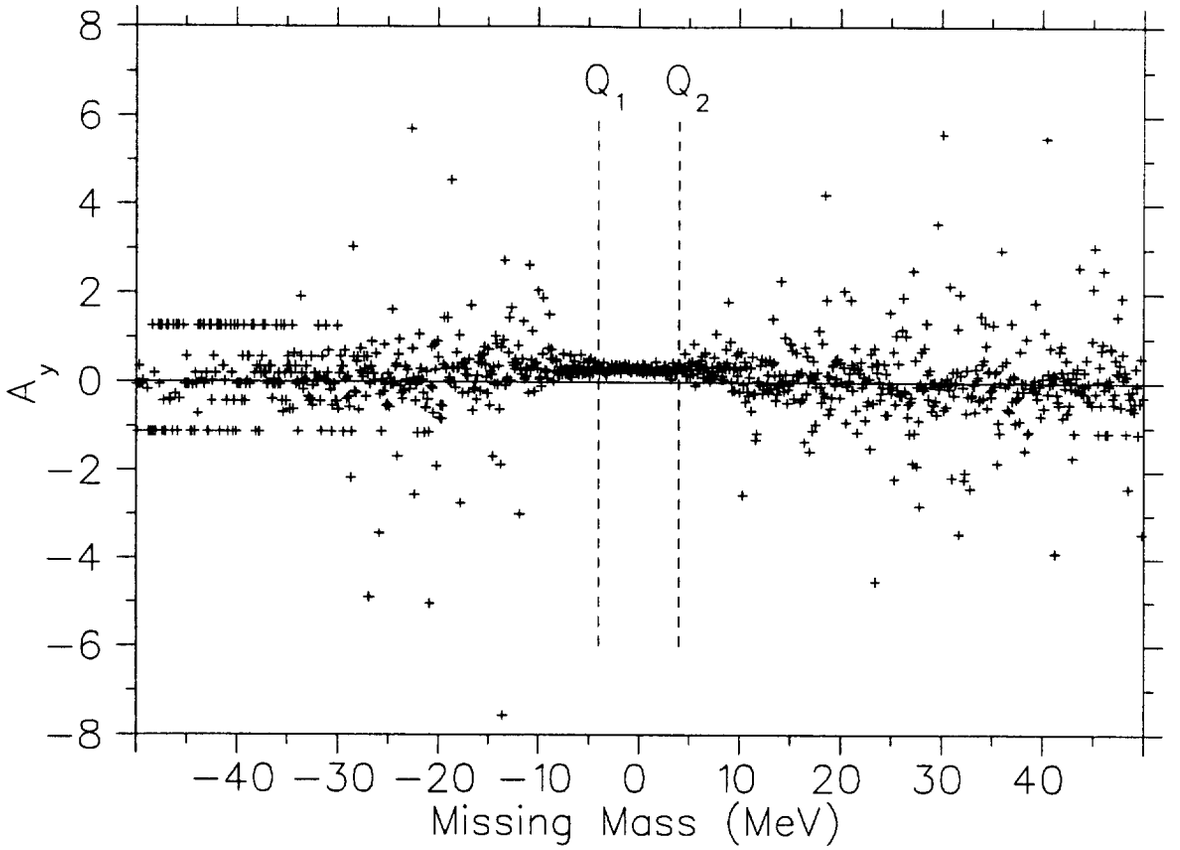

FIG. 8. Gaulard, "Analyzing powers..."; PRC

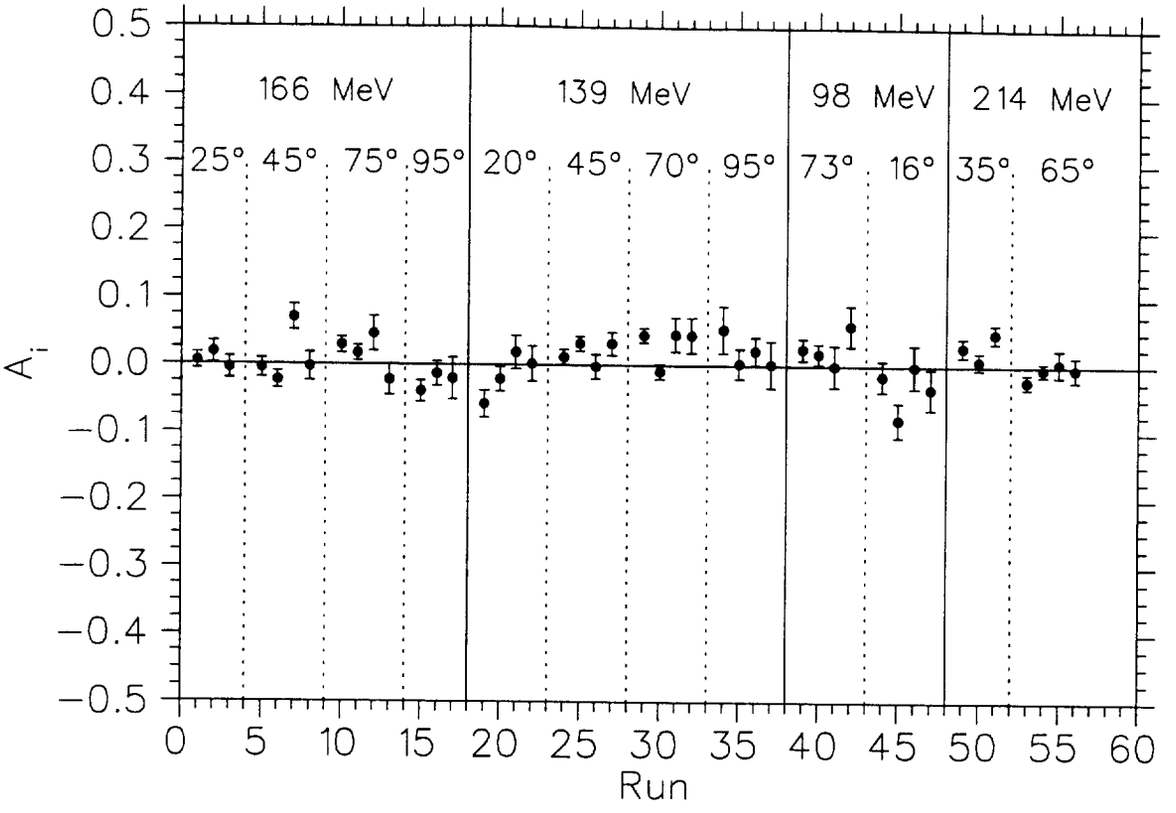

FIG. 9. Gaulard, "Analyzing powers..."; PRC

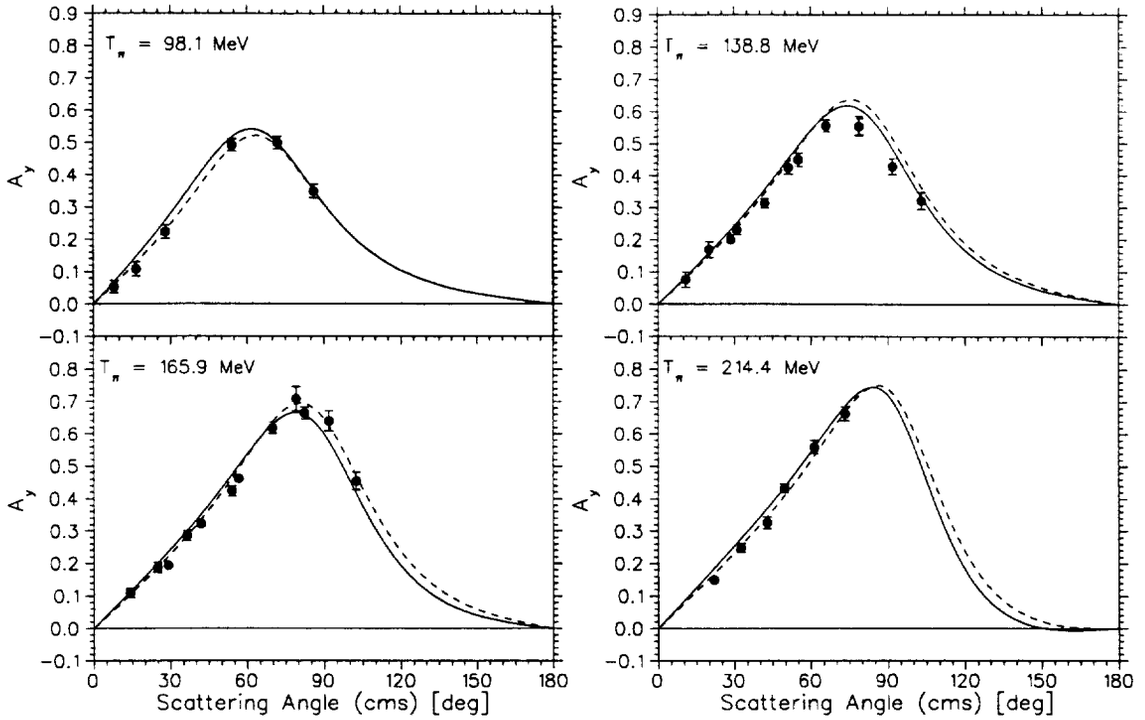

FIG. 10. Gaulard, "Analyzing powers..."; PRC